RSC Advances

PAPER

View Article Online
View Journal | View Issue

Cite this: *RSC Adv.*, 2024, **14**, 4556

A signal "switch-on" photoelectrochemical sensor based on a 3D-FM/BiOI heterostructure for the sensitive detection of L-ascorbic acid†

Huijun Guo, * Xin Wang, Shihao Wang, Hanyu Ma and Jianzhi Liu

Received 5th December 2023
Accepted 17th January 2024

DOI: 10.1039/d3ra08288a

rsc.li/rsc-advances

A highly efficient 3D flower MoS_2 (3D-FM)-based heterostructure photocatalyst (3D-FM/BiOI) was successfully obtained *via* a simple hydrothermal synthesis strategy. 3D-FM/BiOI showed prominent photoelectrochemical performance, distinguished stability and good selectivity. The introduction of 3D-FM, by promoting the photoelectric property attributed to it, facilitated the separation of photogenerated electron–hole pairs. Since the redox process of L-ascorbic acid (L-AA) resulted in an increasing photocurrent of 3D-FM/BiOI, a signal "switch-on" photoelectrochemical sensor (PECS) was designed to sensitively determine L-AA for the first time. Under optimized conditions, the 3D-FM/BiOI PECS worked over a wide range from 1 μM to 0.8 mM with a low detection limit of 0.05 μM (S/N = 3). The PECS was successfully exploited for L-AA sensing in human urine with excellent accuracy and applicability, demonstrating its practical precision and superb serviceability. Furthermore, the 3D-FM/BiOI PECS exhibited satisfactory selectivity and stability, providing a great potential platform for the construction of an L-AA sensor in various practical samples and complicated environments.

1 Introduction

As a crucial component in biological metabolism, L-ascorbic acid (L-AA) is present in many bodily fluids and participates in several biological processes of great relevance.[1] Furthermore, it is significant to the immune response and prevents free-radicals, such as those found in cancer and Parkinson's disease.[2] Many fruits and vegetables contain L-AA, especially beverages derived from fruit juice. In the presence of heat, light and iron, the air-oxidation rate of L-AA is sharply accelerated.[3] However, humans cannot self-synthesize it. Therefore, the development of a facile and rapid analytical method for the sensing of L-AA with high selectivity and sensitivity is particularly crucial in diagnostic applications and the pharmaceutical field.[4,5]

To date, several traditional methods, such as liquid chromatography,[6] fluorescence,[7] chemiluminescence and electrochemical methods,[8] have been exploited for the determination of L-AA. Among these analytical methods, photoelectrochemical (PEC) detection[9] is a brand-new approach to a sensing platform for biochemical molecules, which is attributed to electron transfer between target, photocatalyst and electrode with photo-irradiation.[10] It integrates electrochemical and optical techniques to analyze the concentration of target analytes. Due to their electrochemical detection in conjunction with photo-irradiation, PEC[11] sensors present some excellent properties, such as low background noise, and simple sample processing and operation.[12] Inorganic semiconductors possess exceptional photoelectric conversion efficiency and are widely adopted photoelectric materials for constructing PEC sensors.

BiOX (X = Cl, Br, I) are p-type semiconductors and eminent photocatalyst materials, attributed to their pertinent band gaps and unique tetragonal crystal structure with a strong internal electric field, which can increase the effective separation of electron–hole pairs.[13] Bi oxides with a band gap ranging from 1.8 to 3.0 eV yield high photocatalytic efficiency under visible light irradiation.[14] Among Bi oxides, bismuth oxyhalides (BiOX, X = Br, Cl, I) with their great electrochemical and optical properties have attracted growing attention in modern applications such as photocatalysis[15] and optoelectronic devices.[16] Bi oxyhalides are characterized by a unique layered structure which makes them the dominant family of photoactive materials under visible light irradiation. The electrical field between $[Bi_2O_2]^{2+}$ sheets and X slabs inhibits electron–hole recombination, which can increase the photocatalytic performance. Among BiOX catalysts, bismuth oxyiodide (BiOI) has been the subject of growing attention due to its narrow band gap (1.7–1.8 eV) and effective visible-light activity.

Recently, many important studies have been reported into BiOX, such as photocurrent-polarity switching between methylene-blue-loaded liposome and iodine-doped BiOCl for *in situ* amplified immunoassay[17] and ultrathin mesoporous BiOCl nanosheet-mediated liposomes for photoelectrochemical immunoassay with *in situ* signal amplification.[18] BiOI with its

Center of Characterization and Analysis, Jinlin Institute of Chemical Technology, Jilin 132000, China. E-mail: m15981210065@163.com

† Electronic supplementary information (ESI) available. See DOI: https://doi.org/10.1039/d3ra08288a

layered structure and strong internal electric field shows the best visible light response with a relatively narrow band gap compared with other BiOX (Cl or Br).[19] Unfortunately, BiOI still exhibits some disadvantages of slow separation of photo-generated electron–hole pairs and the limitation of its band structure.[20] To overcome these shortcomings, many approaches have been employed to modify BiOI to extend the lifetime of charge carriers, including morphological modulation[21] and combination with other semiconductors.[22] Therefore, various attempts, including co-catalysts, constructing heterostructures and doping, have been exploited to enhance its property. Constructing heterogeneous structures has been reported to be an effective approach, such as constructing g-C_3N_4/BiOI,[23] BiOI/Bi_2MoO_6 nanocomposite[24] and BiOI/graphene hydrogel.[25]

A 3D-FM construction composed of 2D nanosheets is supposed to be a particularly good catalyst for practical applications,[26] which not only increases its structural stability but also maximizes the exposure of its active sites. It possesses high charge mobility, a large specific surface area and excellent photo-electron conversion with wide application in photocatalysis,[27] dry lubrication,[28] lithium batteries,[29] and hydrogen production.[30] Furthermore, 3D-FM plays a crucial role in photocatalysis and photoelectrochemistry. It is reported that 3D-FM can form a heterojunction with semiconductors such as Cu_2O/3D-FM nanohybrid,[31] In_2O_3/3D-FM nanofilm[32] and Nafion/hemoglobin/3D-FM.[33] Nevertheless, to the best of our knowledge, there have been few reports exploring the application of MoS_2/semiconductor heterostructures for PEC sensing.

In this work, 3D-FM/BiOI composites were successfully synthesized through a facile and convenient one-step solvent thermal method, which exhibited much stronger photoactivity than BiOI. The 3D-FM/BiOI photocatalysts displayed greatly improved photocatalytic performance under visible light. The intimate interfacial contact between 3D-FM and BiOI nanosheets promoted charge separation efficiency. A 3D-FM/BiOI heterojunction-based PEC sensing system can promote the transfer of interfacial charges and improve the separation of photo-generated electron–hole pairs. A signal "switch-on" PECS was designed to sensitively determine L-AA, based on the redox process of L-AA. The enhanced activity was ascribed primarily to the formed heterostructure, which can promote the transfer of interfacial charges and improve the separation of photo-generated electron–hole pairs. The results showed that 3D-FM/BiOI exhibited excellent sensitivity, selectivity and stability, and the performance of the 3D-FM/BiOI sensor was superior to that of most reported sensors. To further verify its practical applicability, the established sensor was applied for L-AA detection in human urine samples. This work will provide inspiration to scientific researchers to construct photoelectrochemical sensors using heterostructure materials that will have potential application value.

2 Experimental section

2.1. Synthesis of the photocatalysts

All reagents were chemical analysis grade and there was no further purification for the experiments.

2.1.1 Synthesis of 3D-FM. All 3D-FM hemispheres were synthesized by a facile hydrothermal method.[34] First, 7 mmol of thiourea (H_2CSNH_2), 0.25 mmol of ammonium molybdate $(NH_4)_6Mo_7O_{24}\cdot 4H_2O$, and 1 mmol of hexadecyltrimethylammonium bromide (CTAB) were all diffused in 10 mL of ultrapure water to form a well-distributed solution. Then, the well-distributed solution was kept in a state of intense agitation until the addition of ammonia solution (3 M) adjusted the pH to the appropriate value. Subsequently, the obtained solution was transferred into a 25 mL Teflon-lined autoclave and heated at 200 °C for 24 h. The powdered product was obtained after naturally cooling down to room temperature. It was washed several times with analysis-grade ethanol and ultrapure water. Finally, the product was dried at 60 °C for 12 h to obtain the pure product.

2.1.2 Preparation of 3D-FM/BiOI. 3D-FM/BiOI was fabricated according to a previous report[35] with some modification. First, 0.1 g of the obtained 3D-FM was added into a solution of $Bi(NO_3)_3\cdot 5H_2O$ in ethylene glycol (60 mL, 0.10 M). After the mixture had formed a homogeneous suspension under ultrasound, KI ethylene glycol solution (60 mL, 0.20 M) was added drop by drop into the above mixture with vigorous stirring. The above mixture solution was kept under stirring for 1 h and then transferred to a 100 mL Teflon-lined autoclave. It was heated to 160 °C for 12 h. Subsequently, the product was washing alternately with ethanol and ultrapure water. Finally, the solid was dried at 60 °C for 4 h to obtain 3D-FM/BiOI pure product.

For comparison, pure BiOI was synthesized by the above method without adding 3D-FM.

2.2. Preparation of 3D-FM/BiOI/ITO electrodes

ITO electrodes were cleaned with acetone, isopropanol, ethanol, and deionized water in sequence for 30 min each under ultrasonic conditions, then dried at 60 °C for 2 h. Then, 10 mg of the prepared 3D-FM/BiOI and 20 μL of Nafion (5 wt%) were added to 1 mL of ultrapure water, and then subjected to ultrasonic waves for 1 h to obtain a 10 mg mL^{-1} 3D-FM/BiOI suspension. Next, 50 μL of suspension was dropped onto the clean ITO, and dried at room temperature to obtain a 3D-FM/BiOI electrode. For comparison, individual suspensions of pure BiOI and 3D-FM were dropped onto ITO to give 3D-FM/ITO and BiOI/ITO by the above method.

2.3. PEC measurements

The PEC properties were measured with an electrochemical workstation (CHI 760E, Shanghai Chenhua Instrument Corporation, China) in a standard three-electrode system. An Ag/AgCl electrode in 3 M KCl, a Pt plate and 3D-FM/BiOI/ITO were exploited as the reference electrode, counter electrode and working electrode, respectively. The electrochemical behavior of 3D-FM/BiOI/ITO was investigated at different scanning speeds. A 20 W xenon lamp provided simulated sunlight (Beijing Newbet Technology Co., Ltd, China) and 0.1 M phosphate buffer solution (PBS, pH = 7.4) was used as the electrolyte. Cyclic voltammetry (CV) curves were performed from −0.2 V to 0.6 V *vs.* Ag/AgCl at a scan rate of 50 mV s^{-1}. Electrochemical

impedance spectroscopy (EIS) was conducted in 0.1 M KCl solution containing 0.5 mM of $K_3Fe(CN)_6/K_4Fe(CN)_6$ at −0.2 V *vs.* a reversible hydrogen electrode (RHE) with a small-amplitude alternating current of 10 mV in the frequency range from 0.1 Hz to 100 kHz. The PEC tests for L-AA were performed at a bias potential of −0.228 V (*vs.* saturated Ag/AgCl).

3 Results and discussion

3.1. Characterization of the synthesized materials

The morphology and elemental distribution of BiOI, 3D-FM and 3D-FM/BiOI were observed by scanning electron microscopy (SEM) and energy-dispersive X-ray spectroscopy (EDS). The microstructure of BiOI showed a regular spherical structure and a diameter of approximately 2–3 μm (Fig. 1a). The high-magnification image of the 3D-FM hemispheres showed that the uniform 2D nanosheet petals are arranged together in a disorganized and staggered manner, which could effectively inhibit the aggregation of a single 3D-FM nanosheet (Fig. 1b). The micrograph of BiOI showed it was attached closely to the surface of 3D-FM (Fig. 1c), indicating the form of the 3D-FM/BiOI heterostructure. Fig. 1d shows the EDS region of the 3D-FM/BiOI composite and its corresponding EDS mappings (Fig. 1e–i), which demonstrate that there are only Bi, O, I, Mo and S elements in the 3D-FM/BiOI composite and the BiOI are evenly distributed. To further investigate the morphological and structural information for the 3D-FM/BiOI composite, the TEM of BiOI and the 3D-FM/BiOI composite were analyzed, as shown in Fig. 2a and b, and the elemental distributions were observed with energy-dispersive X-ray spectroscopy (EDS) (c–g). The HRTEM of 3D-FM/BiOI was analyzed, and the results are shown in Fig. S1a and b,† and different lattice fringes are found.

The crystalline structures of BiOI, 3D-FM and 3D-FM/BiOI were identified by X-ray diffraction (XRD). The XRD pattern of 3D-FM was consistent with that reported in the literature.[36] As shown in Fig. 3, the diffraction peaks of the tetragonal phase of BiOI were consistent with the diffraction peaks of (012), (110), (014) and (212) in the composites. The XRD pattern of the 3D-FM/BiOI heterostructure showed predominantly the main peaks of BiOI and one weak peak (004) of 3D-FM, due to the better crystallinity and stronger peak intensity of BiOI and the small content of 3D-FM.

X-ray photoelectron spectroscopy (XPS) was undertaken to investigate the elemental composition and valence states of the 3D-FM/BiOI composites. Fig. 4 shows the typical survey scan and high-resolution spectra of the Bi (4f, 4d and 4p), Mo 3p, S 2p, O 1s, and I 3d peaks for the 3D-FM/BiOI composites, which are in accordance with the above EDS result. Bi, O, and I elements related to BiOI and the Mo, O, and S elements related to 3D-FM were observed in the survey XPS of 3D-FM/BiOI, illustrating that BiOI was successfully attached to 3D-FM. Fig. 5a clearly shows the binding energy of Bi 4f, in which the two peaks located at 165 eV and 156.5 eV are the characteristic peaks of Bi $4f_{5/2}$ and Bi $4f_{7/2}$ in 3D-FM/BiOI, suggesting that the chemical valence state of Bi element in the 3D-FM/BiOI composites is +3.[32] The binding energies of I $3d_{3/2}$ and I $3d_{5/2}$ in 3D-FM/BiOI are located at 616 eV and 627.5 eV, respectively (Fig. 5d). This is the characteristic peak of I^- in the 3D-FM/BiOI samples. For the O 1s spectrum (Fig. 5b), the peaks for the Bi–O bond (527.1 eV) and I–O bond (529.5 eV) were ascribed to BiOI. The peak of S 2P was exhibited in the spectrum of Bi + S (Fig. 5a). However, the existence of Mo indicates that 3D-FM had been successfully introduced into the composite (Fig. 5c). The above XPS analysis confirmed the successful fabrication of a 3D-FM/BiOI heterojunction.

The bonding and chemical composition of BiOI and the 3D-FM/BiOI composites were investigated using FT-IR spectra. From Fig. 6, the band at about 3425 cm^{-1} is the stretching vibration of O–H, which is the deformation vibration of absorbed water molecules.[35] The band at 498 cm^{-1} corresponds to the stretching mode of Bi–O, which results from BiOI. With

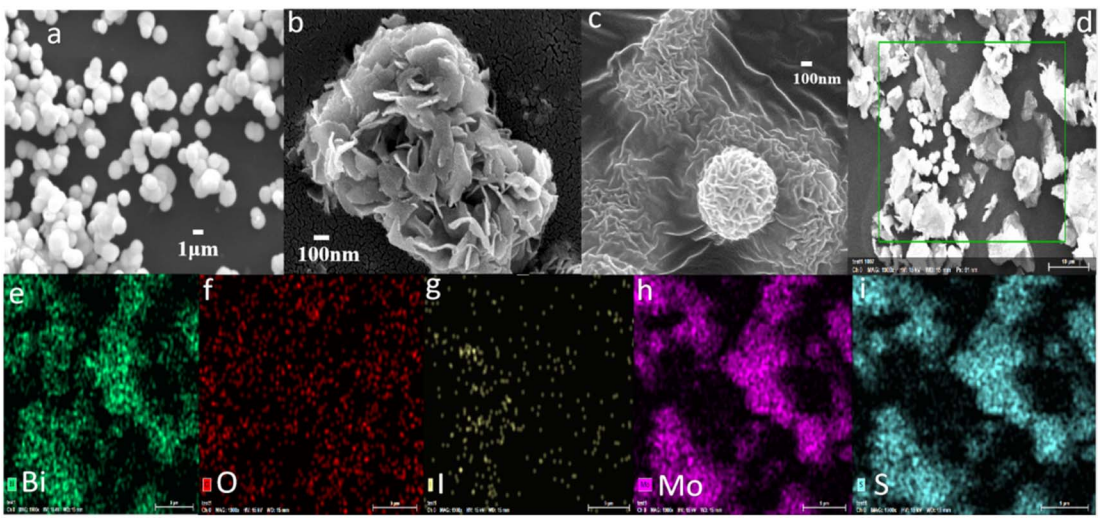

Fig. 1 The SEM morphology of (a) BiOI, (b) 3D-FM and (c) 3D-FM/BiOI. (d) The energy-dispersive X-ray spectroscopy (EDS) region of the 3D-FM/BiOI composite and its corresponding EDS mappings (e–i).

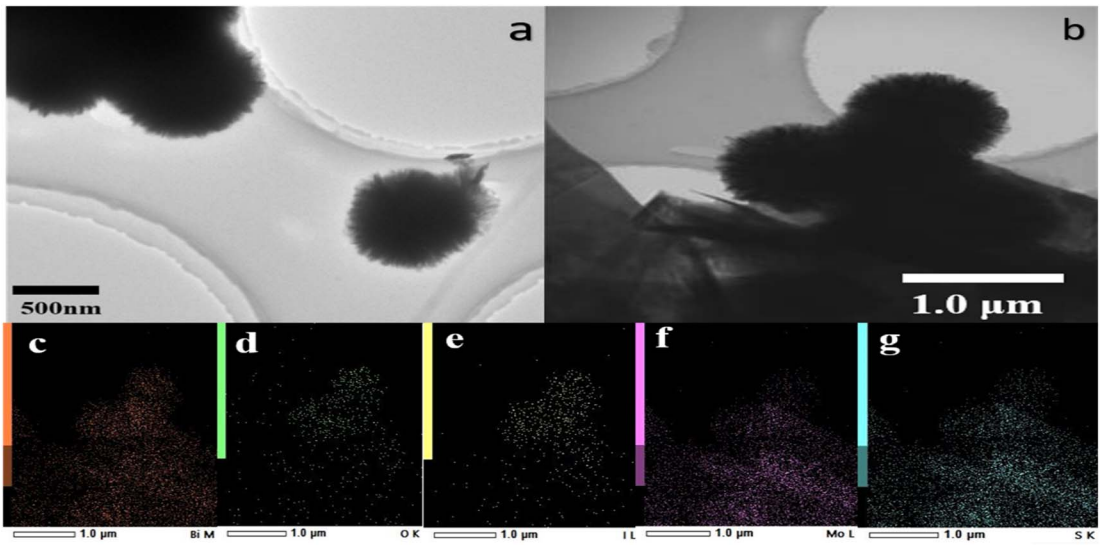

Fig. 2 The TEM morphology of BiOI (a) and (b) 3D-FM/BiOI. (c–g) The elemental distribution observed with energy-dispersive X-ray spectroscopy (EDS).

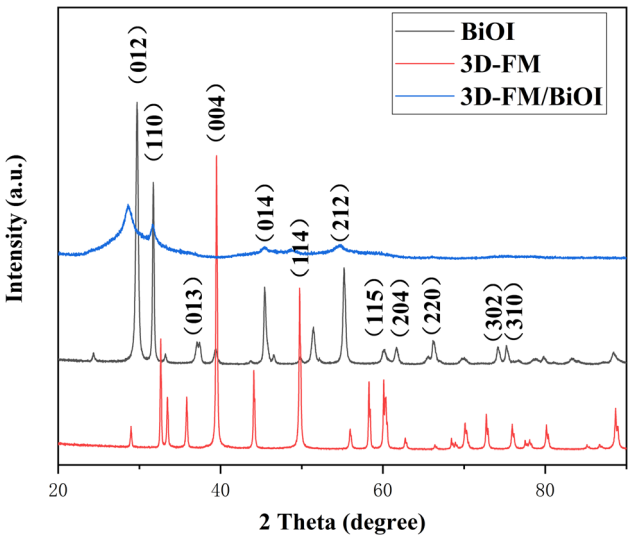

Fig. 3 The X-ray diffraction patterns of BiOI, 3D-FM and 3D-FM/BiOI.

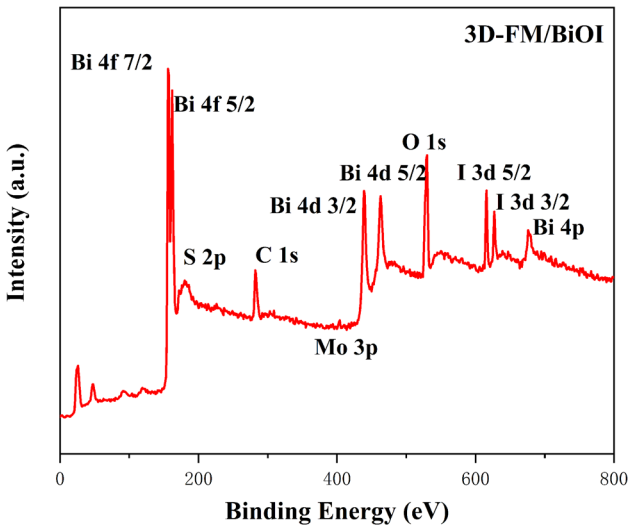

Fig. 4 XPS spectra of 3D-FM/BiOI.

increasing 3D-FM content, the peak of the 3D-FM/BiOI composites at 498 cm^{-1} is shifted slightly compared with pure BiOI. This proves the interaction of 3D-FM nanosheets and BiOI nanosheets, which formed an excellent heterojunction structure. The FT-IR results are in accordance with the XRD analysis, and indicate that the 3D-FM has been successfully coupled with BiOI.

3.2. Sensing mechanism of the 3D-FM/BiOI sensing system

Hydroxyl radicals ($^{\bullet}OH$) and photogenerated holes (h^{+}) are the major active factors in the process of photocatalytic oxidation. Similar research has been reported, such as a contactless photoelectrochemical biosensor based on the ultraviolet-assisted gas sensing interface of 3D-SnS_2 nanosheets[37] and the photoelectrochemical bioanalysis of microRNA on yolk-in-shell Au@CdS based on a catalytic hairpin-assembly-mediated CRISPR-Cas12a system,[38] *etc.*[39,40] According to the properties of semiconductors, p-type semiconductors enter the solution with holes under light, and electrons enter the counter electrode.[41,42] The electron donor consumes the holes, and the electron donor undergoes an oxidation reaction. In contrast, n-type semiconductors enter the solution under light, and holes enter the counter electrode. The electron acceptor consumes electrons in the solution, and the electron acceptor undergoes a reduction reaction. Above all, L-AA is easily oxidized and generally serves as an electron donor, and so serves as a hole scavenger. The probable mechanism of 3D-FM/BiOI as a photocatalyst was explored for an increase in photocatalytic capabilities and detecting the content of L-AA (Fig. 8). The minimum

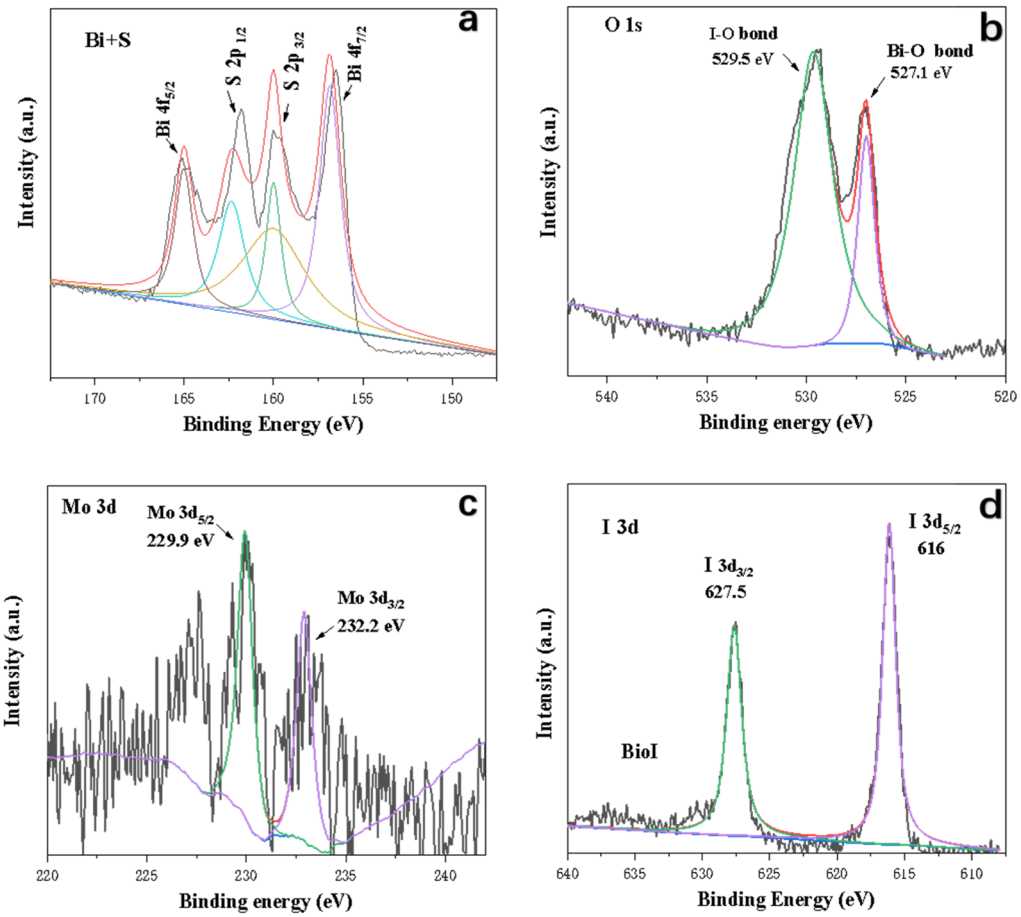

Fig. 5 Survey spectra and high-resolution core spectra for (a) Bi + S, (b) O 1s, (c) Mo and (d) I 3d.

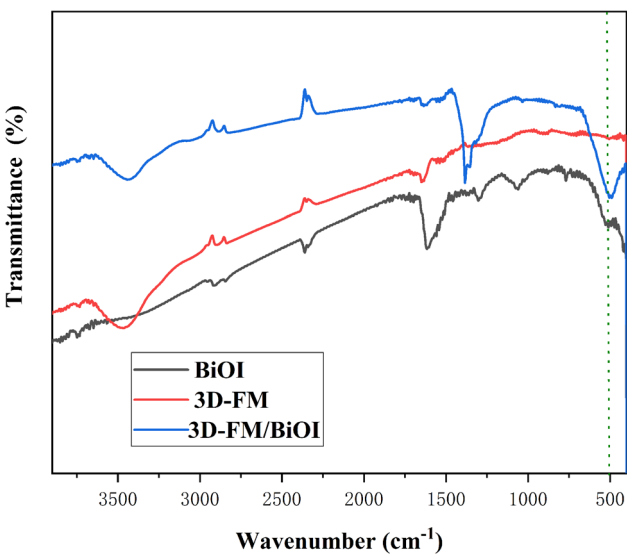

Fig. 6 The FT-IR spectra of BiOI and 3D-FM/BiOI.

position of the conduction band (CB) and the maximum position of the valence band (VB) of BiOI and 3D-FM are estimated by employing the empirical formulae:

$$\mathrm{EVB} = X - E_e + 0.5E_g \quad (1)$$

$$\mathrm{ECB} = \mathrm{EVB} - E_g, \quad (2)$$

where X is the absolute electronegativity, which is 5.94 eV. E_e is a constant of the free electrons energy with respect to the hydrogen scale ($\approx$4.5 eV), and E_g is the forbidden bandwidth of a semiconductor. On the basis of the UV-vis spectra, the band gap energy of BiOI nanosheets is 1.38 eV (Fig. 7a). Therefore, the calculated EVB and ECB of BiOI are 2.13 and 0.75 eV, respectively. According to the Nernst equation (eqn (3)), the EVB (*vs.* NHE, pH = 7.4) and ECB (*vs.* NHE, pH = 7.4) of BiOI were calculated to be 1.69 V and 0.31 V, respectively.

$$E(\mathrm{NHE, pH} = 7.4) = E(\mathrm{NHE, pH} = 0) - 0.059\ \mathrm{pH} \quad (3)$$

Furthermore, the Fermi level (EF) of the 3D-FM nanosheets (0.41 eV) (Fig. 7b) is more positive than the CB potential of BiOI, which favors the transfer of photoelectrons on the VB of BiOI to 3D-FM through the heterojunction interface, thereby promoting the separation of photocarriers.

Under visible light irradiation (λ > 400 nm), the photogenerated electrons on the VB are excited and transferred to the corresponding CB, and the holes are left on the valence band of

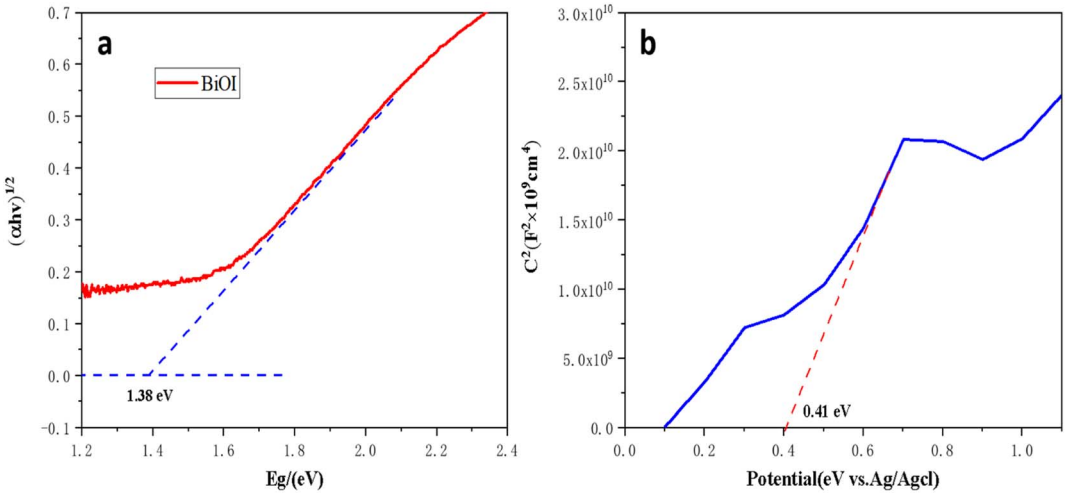

Fig. 7 (a) The photon energy ($h\nu$) for BiOI and (b) the Fermi level (EF) of 3D-FM nanosheets.

BiOI and 3D-FM nanosheets. Because the CB potential of 3D-FM is more negative than that of BiOI, the photo-induced electrons on the CB of 3D-FM can easily transfer to the CB of BiOI through the interface. At the same time, the VB position of 3D-FM is more negative than that of BiOI, so the holes can migrate from BiOI to the 3D-FM nanosheets; thus the efficient separation of photogenerated carriers occurs.

L-AA is an effective hole capture agent in photoelectric detection. The 3D-FM/BiOI PEC sensor is a kind of target-analyzing device based on a photoelectrically active material. When the light is on, the electrons in the 3D-FM/BiOI material are excited, and the identifying probe on the material captures L-AA, causing a change in photocurrent or photovoltage. The photoelectric signal changes with the concentration of L-AA, and there is a functional relationship between the two. Therefore, the change in the photoelectric signal can be used to quantitatively determine the L-AA. The valence band potential of the photocatalysts of the 3D-FM/BiOI composite is much higher than the oxidation potential of L-AA (+0.153 eV). When 3D-FM/BiOI/ITO is stimulated by light, L-AA can easily be oxidized by holes to dehydroascorbic acid (DHA), and the hydrogen ions gain electrons and will be reduced to H_2 at the opposite electrode. In this process, L-AA acts as a hole scavenger by providing electrons to the photocatalysts of the 3D-FM/BiOI composite, reducing the recombination of the electron–hole pair and enhancing the photocurrent signal. The PEC sensing mechanism on L-AA may follow eqn (4)–(6):

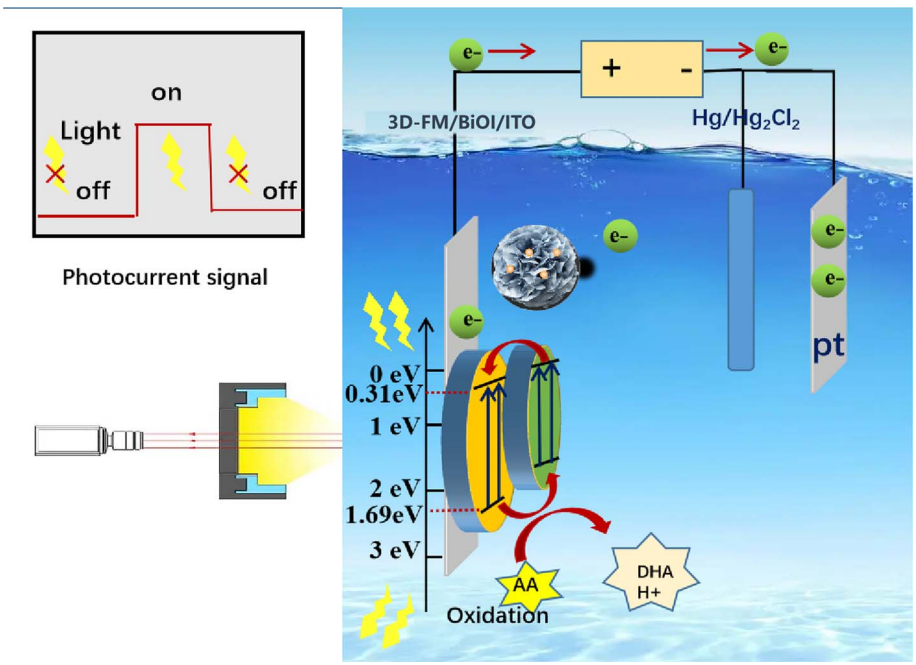

Fig. 8 The probable mechanisms of 3D-FM/BiOI as photocatalysts under visible light.

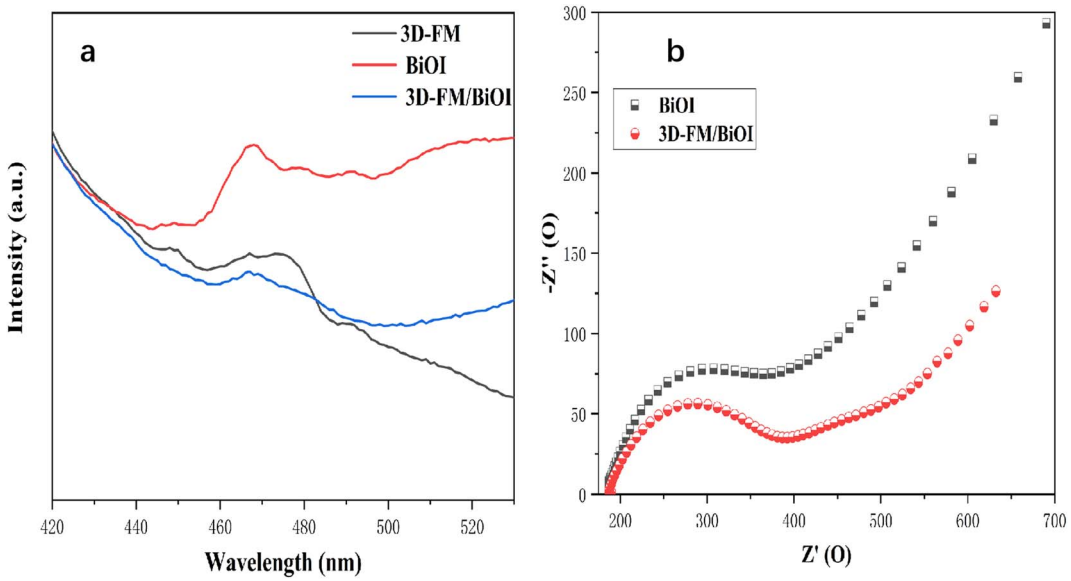

Fig. 9 (a) Photoluminescence emission spectra of (a) 3D-FM, BiOI and 3D-FM/BiOI. (b) EIS plots of BiOI and 3D-FM/BiOI/ITO.

$$\text{BiOI/3D-FM} + h\nu \rightarrow \text{BiOI/3D-FM} + h^+ + e^- \quad (4)$$

$$\text{L-AA} + h^+ \rightarrow \text{DHA} + H^+ \quad (5)$$

$$4H^+ + 4e^- \rightarrow 2H_2 \quad (6)$$

The separation rate of electrons and holes determines the effect of the photocatalytic activity. Weak PL peaks represented low recombination rates of photo-excited electrons and holes. PL spectra of BiOI, 3D-FM and BiOI/3D-FM with an excitation wavelength of 350 nm (Fig. 9a) showed that the peaks of BiOI/3D-FM samples are lower than those of BiOI and 3D-FM, which suggested that the recombination of electrons and holes is restrained due to the formation of a heterojunction between BiOI and 3D-FM. The sample of BiOI/3D-FM had the lowest PL intensity among all the samples, which indicated the heterojunctions and surface-active oxygen between BiOI and 3D-FM. The cooperative effect of the above two factors caused it to have higher migration efficiency of photoelectron and hole pairs, which improved the ability for photocatalytic performance.

3.3. Characteristics of PEC sensing

The electrochemical property of the 3D-FM/BiOI electrode was further explored with the CV curves (Fig. 10a) in 1.0 M KCl solution containing 5.0 mM $[Fe(CN)_6]^{3-/4-}$. 3D-FM/BiOI exhibited almost no significant variation in redox peak current compared to that in pure BiOI, which may be attributed to the addition of a small amount of 3D-FM.

The relationship between the enhanced photocurrent and charge transfer was investigated by EIS. The semicircle in an EIS plot can reveal the charge transfer resistance. As depicted in Fig. 9b, 3D-FM/BiOI/ITO exhibited a smaller arc size than BiOI and the calculated charge transfer resistance value of 3D-FM/

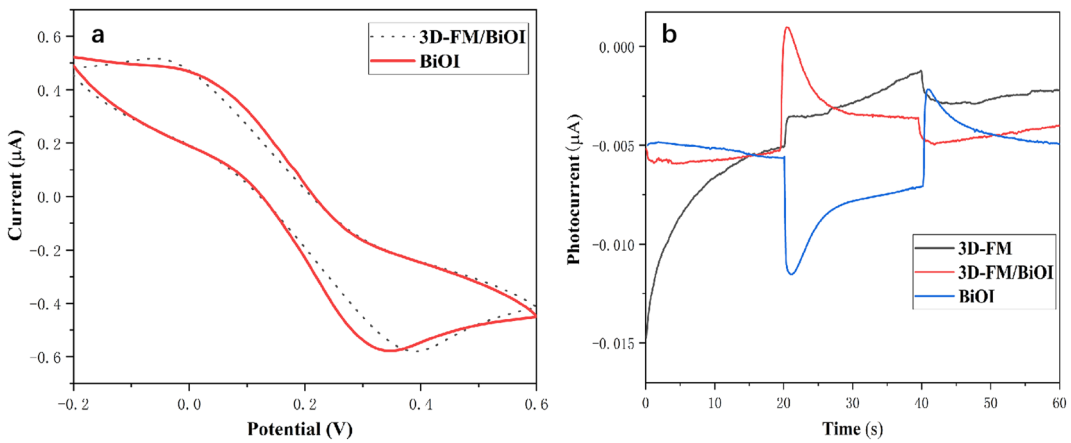

Fig. 10 (a) CV curves of 3D-FM/BiOI and pure BiOI. (b) Photocurrent of 3D-FM/BiOI, BiOI and 3D-FM under visible light illumination.

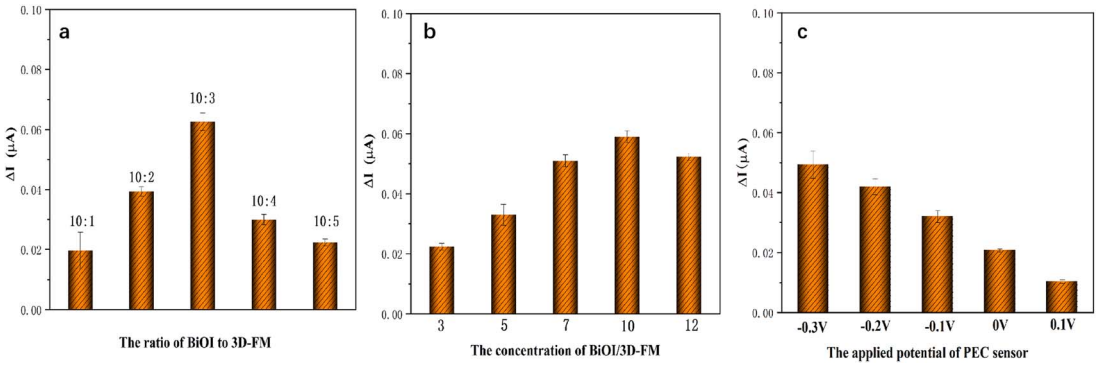

Fig. 11 The effects of (a) the ratio of BiOI to 3D-FM; (b) concentration of BiOI/3D-FM; (c) applied potential. Conditions: (a) concentration: 10 mg mL^{-1}; applied potential, −0.2 V; (b) the ratio of BiOI to 3D-FM, 10 : 3; applied potential, −0.2 V; (c) the ratio of BiOI to 3D-FM, 10 : 3; concentration, 10 mg L^{-1} (All experiments were conducted in 0.1 M PBS (pH 7.4) containing 1 μM L-AA.).

BiOI (200.5 Ω) was also smaller than that of BiOI (275 Ω). These results further confirmed that the introduction of 3D-FM could promote charge transfer and reduce overall charge transfer resistance, which plays an important role in enhancing the photocurrent.

Under visible light illumination, the PEC properties of 3D-FM, BiOI and 3D-FM/BiOI were explored to evaluate the transient photocurrent response by estimating 60 s photocurrent curves. As shown in Fig. 10b, 3D-FM exhibited a weak anode photocurrent, while BiOI as a p-type semiconductor showed an extremely weak cathode photocurrent owing to its relatively narrow band gap (1.95 eV), which makes the electrons and holes easy to recombine. After introducing 3D-FM into BiOI, a remarkably improved photocurrent response was observed for the 3D-FM/BiOI electrode, which was several times larger than that of BiOI. The sensitive photocurrent response is attributed to the effective separation and transmission of photocarriers in 3D-FM/BiOI, which is due to the excellent conductivity of multilayer 3D-FM and the strong interface connection between 3D-FM and BiOI.

3.4. Optimization of experimental conditions

All optimization of experimental conditions was conducted in 0.1 M PBS (pH 7.4) containing 1 μM of L-AA. To achieve optimal performance of the PEC sensor, a study of the influence of the ratio of BiOI to 3D-FM was conducted. When the ratio of BiOI to 3D-FM was significantly increased from 10 : 1 to 10 : 3, the photocurrent difference also significantly increased. However, when the ratio was further increased to 10 : 4, the photocurrent difference increased only slowly (Fig. 11a). This is because the introduction of 3D-FM can enhance the photoelectric activity, but it is not conducive to the oxidation of L-AA. Therefore, the optimal ratio of 3D-FM to BiOI was 10 : 3 and this was selected for the sensing experiments.

The influence of the concentration of 3D-FM/BiOI was then explored. When the concentration of BiOI/3D-FM was varied from 3 to 12 mg mL^{-1}, the photocurrent difference was greatly enhanced (Fig. 11b). When the concentration was further increased from 10 to 12 mg mL^{-1}, a significant decrease in photocurrent difference was exhibited. The decline was due to the thicker coating on the surface of ITO hindering electron

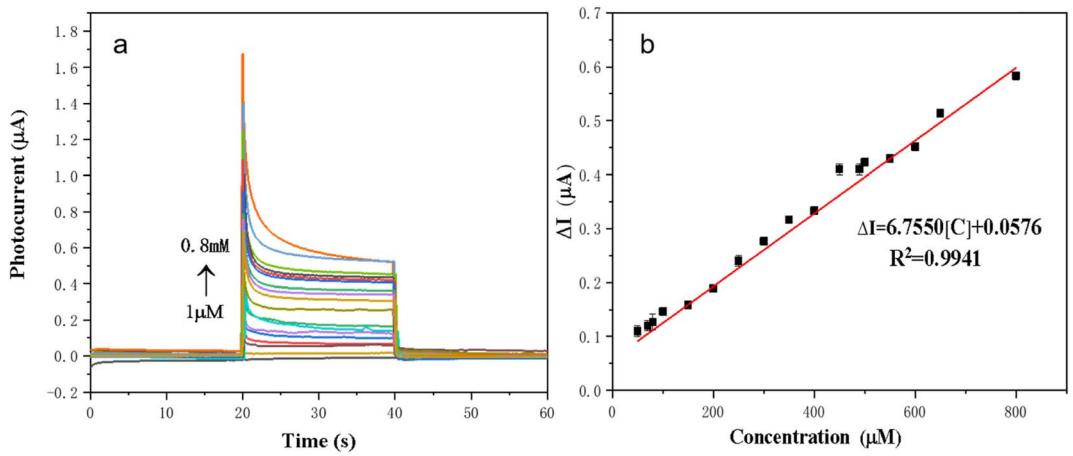

Fig. 12 (a) PEC responses of the BiOI/3D-FM sensor at different L-AA concentrations. (b) The corresponding calibration curve for the determination of L-AA.

Table 1 Recovery of L-AA in human urine by 3D-FM/BiOI/ITO photoelectric detection[a]

Sample	Determined (μM)	Spiked (μM)	Found (μM)	Recovery (%)	RSD (%)
1	0.45 ± 0.01	5	4.82	96.40	4.32
2	0.43 ± 0.01	20	21.3	106.50	3.05
3	0.47 ± 0.03	100	101.5	101.5	2.63

[a] RSD (%) = (standard deviation/the average of the data obtained by repeating 3 times) × 100%.

transfer, thereby affecting the oxidation of L-AA and leading to a decrease in the photocurrent difference. Thus, 10 mg mL^{-1} was adopted as the appropriate concentration of 3D-FM/BiOI for the subsequent experiments.

The applied potential of a PEC sensor can affect the amplitude of the photocurrent. A more negative application potential leads to a stronger cathode photocurrent and electron drift caused by larger measurement bias. Furthermore, the effect of an applied potential ranging from −0.3 V to 0 V was investigated. As illustrated in Fig. 11c, the photocurrent difference was greatly enhanced, resulting in the negative shift of the potential. However, a larger applied voltage will lead to a stronger background noise signal, which will interfere with the detection of a low content L-AA. Thus, a bias voltage of −0.2 V was ultimately used in the following experiments.

3.5. Analytical performance of the 3D-FM/BiOI PEC sensing system

The sensing property of the 3D-FM/BiOI sensing platform for accurate detection of L-AA was explored under optimal conditions. As shown in Fig. 12a, the concentration of L-AA increased in the range from 1 μM to 0.8 mM, corresponding to an increase in the photocurrent difference of the 3D-FM/BiOI sensor. Fig. 12b demonstrates that there is a good linear relationship between the concentration of L-AA and photocurrent difference. The linear equation can be described as $\Delta I = 6.7750[C] + 0.0576$ and the coefficient is 0.9941, where ΔI represents the photocurrent difference of L-AA at different concentrations and [C] is the concentration of L-AA. The limit of detection (LOD) calculated from the equation $LOD = 3\sigma/k$ was 0.05 μM, where σ is the standard deviation of the blank solution ($n = 10$) and k is the slope of the linear equation.

3.6. Applications in real sample analysis

To confirm the practicability and feasibility of the developed method, and also to evaluate the applicability of this fabricated photoelectrode for L-AA detection in real human urine samples (as shown in Table 1), in general the standard addition method was used to detect L-AA in a real sample and three repeated experiments were conducted to ensure the authenticity of the data. The urine samples were collected from one male who was 25 years old. Typically, 20 μL of human urine sample was added to 20 mL of 0.1 M PBS (pH 7.4) solution, and then it was measured by the proposed method. To evaluate the accuracy of the analytical result, a recovery test was conducted at three spiked levels (5, 20, 100 μM). The recoveries of L-AA detection in human urine were 96.40–106.50% with a relative standard deviation below 4.32%, indicating the feasibility and good reproducibility of the 3D-FM/BiOI sensor in the detection of human urine samples.

3.7. Selectivity, reproducibility and stability of the 3D-FM/BiOI sensor

The selectivity of 3D-FM/BiOI was explored and investigated in the presence of potential interferents. Sensing solutions including L-AA, dopamine, L-threonine, uric acid, urea, L-arginine and sucrose D-AA were added to the electrolyte to investigate their potential effects on L-AA detection (Fig. 13a). Compared with the photocurrent of 1 μM L-AA, the change in photocurrent was less than 3% after adding 50 μM of

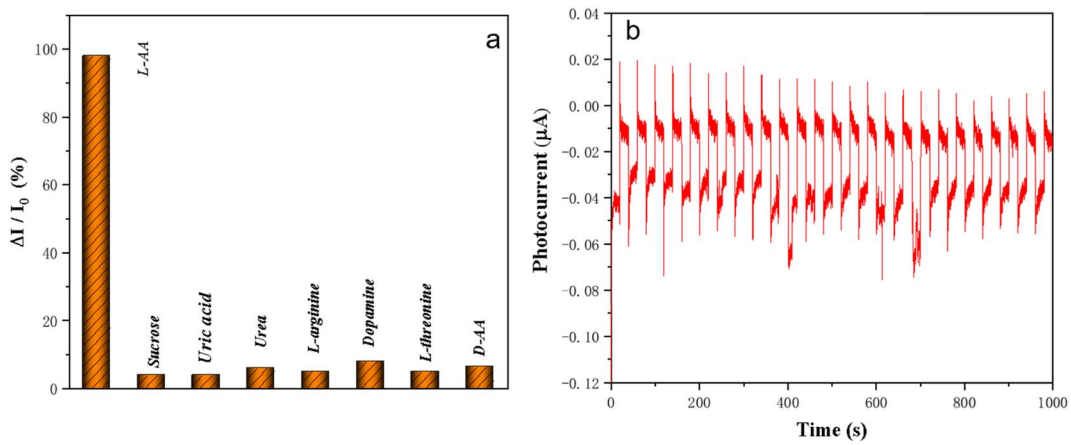

Fig. 13 (a) Evaluation of selectivity of the BiOI/3D-FM sensor to interfering substances. (b) Photocurrent stability of BiOI/3D-FM.

Table 2 Comparison of linear range and detection limit of enzyme-free photoelectrochemical sensors for the determination of L-AA[a]

Modified material	Linear range	Detection LOD	Reference
BiVO4/FTO	5–300 μM	1 μM	**43**
Au/ZnSe/ZnO	0.2–1.8 mM	—	**44**
Dy-OSCN/FTO	7.94 μM–1.113 × 10^{-2} M	3.35 μM	**45**
CoOOH-modified PD	0.1–10 μM	33.4 nM	**46**
CoHCF-modified Pt	1.0 × 10^{-6}–1.0 × 10^{-3} M	1 μM	**47**
g-C_3N_4NSs	0.25–100 μM	—	**48**
This work	1 μM–0.8 mM	0.05 μM	

[a] Dy6-SCN monocrystal: $[Dy_6L2(\mu_3\text{-}OH)_4(\mu_2\text{-}OH)_2(SCN)_8(H_2O)_4]\cdot 6CH_3CN\cdot 2CH_3OH\cdot H_2O$ PDI: perylenediimide CoHCF: cobalt hexacyanoferrate g-C3N4 NSs: graphitic carbon nitride nanosheets.

interferents to the electrolyte with 1 μM of L-AA, which proved that the 3D-FM/BiOI sensor possesses excellent selectivity and anti-interference capability. The good selectivity is attributed to the structure of the 3D-FM/BiOI PEC sensor and the charge generation/transfer mechanism of 3D-FM/BiOI.

The serviceability of 3D-FM/BiOI was estimated according to reproducibility and stability. The experiments were conducted in 0.1 M PBS (pH 7.4) containing 1 μM of L-AA. Different batches of 3D-FM/BiOI were explored, which showed similar PEC performance for the determination of L-AA, demonstrating the good reproducibility of 3D-FM/BiOI. The stability of the 3D-FM/BiOI sensor was investigated by repeating on/off cycles within 1000 s under intermittent visible light irradiation. Fig. 13b shows that the photocurrent can still maintain its initial intensity and there is almost no change after 1000 s. Furthermore, the PEC properties of 3D-FM/BiOI remained unchanged after it was stored at 4 °C in the dark for 7 days. The stability of 3D-FM/BiOI for L-AA was proved by all the results.

3.8. Comparison with other sensors toward L-AA

The analytical performance of the 3D-FM/BiOI PEC sensor toward L-AA was compared with other reported PEC sensors (Table 2). Compared with other reported PEC sensors,[43–48] the established PEC sensor exhibited a wider linear range and much lower LOD for detection of L-AA due to the separated light source and electric detection signal of the PEC sensor, which can effectively reduce the background noise.

4 Conclusions

In summary, a PECS of 3D-FM/BiOI was successfully prepared and applied in sensing L-AA in human urine with excellent accuracy and applicability, demonstrating its practical precision and superb serviceability. Furthermore, the 3D-FM/BiOI PECS exhibited satisfactory selectivity and stability, providing a great potential platform for the construction of an L-AA sensor in various practical samples and complicated environments.

Author contributions

H. G. planned the experiments, conducted the experiments, analyzed the data, and wrote the paper draft. W. X. and S. W. supported and discussed the manuscript. J. L. and H. M. analyzed the data.

Conflicts of interest

The authors declare no conflict of interest.

Acknowledgements

The authors gratefully acknowledge financial support from Jilin Provincial Department of Science and Technology Project [2021020142GX].

References

1 Y. Li, F. Pan, S. Yin, *et al.*, Nafion assisted preparation of prussian blue nanoparticles and its application in electrochemical analysis of l-ascorbic acid, *Microchem. J.*, 2022, **177**, 107278.
2 L. Shen, M. A. Khan, X. Wu, *et al.*, Fe–N–C single-atom nanozymes based sensor array for dual signal selective determination of antioxidants, *Biosens. Bioelectron.*, 2022, **205**, 114097.
3 H. Alhazimeh, M. G. Al-Fandi and L. M. K. Al-Ebbini, Development of an inkjet-printed electrochemical nanosensor for ascorbic acid detection, *Sens. Rev.*, 2022, **42**(3), 342–353.
4 Y. Liu, L. Liang, X. Zhu, *et al.*, N-Doped Carbon Dots as Fluorescent "Turn-Off" Nanosensors for Ascorbic Acid and Fe^{3+} Detection, *ACS Appl. Nano Mater.*, 2022, **5**(5), 7268–7277.
5 A. Singh, K. Kulathuraan, K. Pakiyaraj, *et al.*, Green Synthesized Carbon Quantum Dots from Curcuma Longa for Ascorbic Acid Detection, *Adv. Sci. Technol.*, 2022, **117**, 97–101.
6 L. A. Pachla and P. T. Kissinger, Determination of ascorbic acid in foodstuffs, Pharmaceuticals, and body fluids by liquid chromatography with electrochemical detection, *Anal. Chem.*, 1976, **48**(2), 364–367.
7 Y. N. Wang, S. D. Wang, Y. Fan, *et al.*, A dual-chemosensor based on Ni-CP: Fluorescence turn-on sensing toward

ascorbic acid and turn-off sensing toward acetylacetone, *J. Lumin.*, 2022, **243**, 118680–118685.

8 W. K. Anan, A. Olarnwanich, C. Sriprachuabwong, *et al.*, Disposable paper-based electrochemical sensor utilizing inkjet-printed Polyaniline modified screen-printed carbon electrode for Ascorbic acid detection, *J. Electroanal. Chem.*, 2012, **685**, 72–78.

9 Y. Hou, L. Zhu, H. Hao, *et al.*, A novel photoelectrochemical aptamer sensor based on rare-earth doped Bi_2WO_6 and Ag_2S for the rapid detection of Vibrio parahaemolyticus, *Microchem. J.*, 2021, **165**, 106132.

10 L. P. Tu and G. W. Xu, QDs Based Photoelectrochemical Sensors for Detection of Ascorbic Acid[J], . *Mater Sci Forum*, 2021, **1033**, 77–81.

11 C. T. Hou, J. Y. Peng, Q. Xu, *et al.*, Elaborate fabrication of MOF-5 thin films on a glassy carbon electrode (GCE) for photoelectrochemical sensors, *RSC Adv.*, 2012, **2**, 12696–12698.

12 J. X. Chen and G. C. Zhao, Nano-encapsulant of ascorbic acid-loaded apoferritin-assisted photoelectrochemical sensor for protease detection, *Talanta*, 2017, **168**, 62–66.

13 L. Zhao, X. Zhang, C. Fan, *et al.*, First-principles study on the structural, electronic and optical properties of BiOX (X=Cl, Br, I) crystals, *Physica B*, 2012, **407**(17), 3364–3370.

14 F. Zhang, S. Zou, T. Wang, *et al.*, CeO_2/Bi_2WO_6 Heterostructured Microsphere with Excellent Visible-light-driven Photocatalytic Performance for Degradation of Tetracycline Hydrochloride, *Photochem. Photobiol.*, 2017, **93**(5), 1154–1164.

15 X. Chang, J. Huang, C. Cheng, *et al.*, BiOX (X= Cl, Br, I) photocatalysts prepared using NaBiO 3 as the Bi source: characterization and catalytic performance, *Catal. Commun.*, 2010, **11**, 460–464.

16 A. M. Ganose, M. Cuff, K. T. Butler, *et al.*, Scanlon Interplay of orbital and relativistic effects in bismuth oxyhalides: BiOF, BiOCl, BiOBr, and BiOI, *Chem. Mater.*, 2016, **28**, 1980–1984.

17 H. Y. Wang, X. Y. Wan, X. Wang, *et al.*, Ultrathin mesoporous BiOCl nanosheets-mediated liposomes for photoelectrochemical immunoassay with *in situ* signal amplification, *Biosens. Bioelectron.*, 2023, **239**, 115628.

18 R. J. Zeng, J. H. Xu, T. K. Liang, *et al.*, Photocurrent-polarity-switching photoelectrochemical biosensor for switching spatial distance electroactive tags, *ACS Sens.*, 2023, **8**, 317–325.

19 W. L. Huang and Q. Zhu, DFT calculations on the electronic structures of BiOX (X = F, Cl, Br, I) photocatalysts with and without semicore Bi 5d states, *J. Comput. Chem.*, 2009, **30**(2), 183–190.

20 G. Li, F. Qin, R. Wang, *et al.*, BiOX (X = Cl, Br, I) nanostructures: Mannitol-mediated microwave synthesis, visible light photocatalytic performance, and Cr(VI) removal capacity, *J. Colloid Interface Sci.*, 2013, **409**, 43–51.

21 J. Q. Liu and W. Y. Cheng, Recent Advances in the High Performance BiOX(X=Cl, Br, I) Based Photo-catalysts, *J. Inorg. Mater.*, 2015, **30**(10), 1009.

22 X. Zhang, Z. Ai and F. Jia, etc. Generalized One-Pot Synthesis, Characterization, and Photocatalytic Activity of Hierarchical BiOX (X = Cl, Br, I) Nanoplate Microspheres, *J. Phys. Chem. C*, 2008, **112**(3), 747–753.

23 B. K. Liu, X. L. Han, Y. Wang, *et al.*, Synthesis of g-C_3N_4/BiOI/BiOBr heterostructures for efficient visible-light-induced photocatalytic and antibacterial activity, *J. Mater. Sci.: Mater. Electron.*, 2018, **29**, 14300–14310.

24 W. T. Li, Y. F. Zheng, H. Y. Yin, *et al.*, Heterojunction BiOI/Bi_2MoO_6 nanocomposite with much enhanced photocatalytic activity, *J. Nanopart. Res.*, 2015, **17**(6), 271.

25 D. M. Chen, J. J. Yang, Y. Zhu, *et al.*, Fabrication of bioi/graphene hydrogel/fto photoelectrode with 3d porous architecture for the enhanced photoelectrocatalytic performance, *Appl. Catal., B*, 2018, **233**, 202–212.

26 H. S. Yang, J. Zhou, J. Bao, *et al.*, A simple hydrothermal one-step synthesis of 3d-mos_2/rgo for the construction of sensitive enzyme-free hydrogen peroxide sensor, *Microchem. J.*, 2020, **162**, 105746.

27 P. F. Wang, P. H. Shi, Y. C. Hong, *et al.*, Facile deposition of ag_3po_4 on graphene-like mos_2 nanosheets for highly efficient photocatalysis, *Mater. Res. Bull.*, 2015, **62**, 24–29.

28 P. Serles, K. Gaber and S. Pajovic, High temperature microtribological studies of mos_2 lubrication for low earth orbit, *Lubricants*, 2020, **8**(4), 49.

29 X. S. Zhou, L. J. Wan and Y. G. Guo, Facile synthesis of MoS_2@CMK-3 nanocomposite as an improved anode material for lithium-ion batteries, *Nanoscale*, 2012, **19**, 5868–5871.

30 X. H. Zhang, X. H. Huang, M. Q. Xue, *et al.*, Hydrothermal synthesis and characterization of 3D flower-like MoS_2 microspheres, *Mater. Lett.*, 2015, **148**, 67–70.

31 Y. Liu, X. Xu, J. Zhang, *et al.*, Flower-like MoS2 on Graphitic Carbon Nitride for Enhanced Photocatalytic and Electrochemical Hydrogen Evolutions, *Appl. Catal., B*, 2018, **239**, 334–344.

32 S. Wang, Y. Guan, L. Wang, *et al.*, Fabrication of a novel bifunctional material of BiOI/Ag3VO4 with high adsorption-photocatalysis for efficient treatment of dye wastewater, *Appl. Catal., B*, 2015, **168**, 448–457.

33 T. Yang, Y. Chen, B. Qu, *et al.*, Construction of 3D flower-like MoS2 spheres with nanosheets as anode materials for high-performance lithium ion batteries, *Electrochim. Acta*, 2014, **115**, 165–169.

34 X. Zhang, H. Suo, R. Zhang, *et al.*, Photocatalytic Activity of 3D Flower-like MoS2 Hemispheres, *Mater. Res. Bull.*, 2017, **100**, 249–253.

35 Q. Wang, L. Guo, W. Gao, *et al.*, Facile synthesis of bioi/mxene heterostructure as a superior photoelectrochemical sensor for sensitive detection of glucose, *Anal. Chim. Acta*, 2022, **1233**, 340511.

36 W. H. Zhu, Y. S. Xia, J. X. Xia, *et al.*, Facile synthesis of few-layered mos2 modified bioi with enhanced visible-light photocatalytic activity, *Colloids Surf., A*, 2016, **511**, 1–7.

37 L. T. Huang, G. N. Cai, R. J. Zeng, *et al.*, Contactless photoelectrochemical biosensor based on ultraviolet-assisted gas sensing interface of 3D-SnS2nanosheets: From

mechanism reveal to practical application, *Anal. Chem.*, 2022, **94**, 9487–9495.

38 R. J. Zeng, J. H. Xu, L. L. Lu, *et al.*, Photoelectrochemical bioanalysis of microRNA on yolk-in-shell Au@CdS based on catalytic hairpin assembly-mediated CRISPR-Cas12a system, *Chem. Commun.*, 2022, **58**, 7562–7565.

39 Y. Gao, Y. Y. Zeng, X. L. Liu, *et al.*, Liposome-mediated in situ formation of type-I heterojunction for amplified photoelectrochemical immunoassay, *Anal. Chem.*, 2022, **94**, 4859–4865.

40 Z. C. Yu, H. X. Gong, J. H. Xu, *et al.*, Exploiting photoelectric activities and piezoelectric properties of $NaNbO_3$ semiconductors for point-of-care immunoassay, *Anal. Chem.*, 2022, **94**, 3418–3426.

41 Y. Gao, Y. Y. Zeng, X. L. Liu, *et al.*, Liposome-mediated *in situ* formation of type-I heterojunction for amplified photoelectrochemical immunoassay, *Anal. Chem.*, 2022, **94**, 4859–4865.

42 Z. C. Yu, H. X. Gong, J. H. Xu, *et al.*, Exploiting photoelectric activities and piezoelectric properties of $NaNbO_3$ semiconductors for point-of-care immunoassay, *Anal. Chem.*, 2022, **94**, 3418–3426.

43 L. Li, M. Q. Li, H. Liu, *et al.*, A portable non-enzyme photoelectrochemical ascorbic acid sensor based on $BiVO_4$ electrode under 20 W LED light, *J. Electroanal. Chem.*, 2019, **855**, 113573.

44 X. Wang, G. Li, J. Peng, *et al.*, The Au/ZnSe/ZnO Heterojunction Improves the Electron Transfer Behavior to Enhance the Detection Performance of Ascorbic Acid, *J. Alloys Compd.*, 2021, **873**, 159721.

45 Z. Zhao, D. Han, R. Xiao, *et al.*, An enzyme-free photoelectrochemical sensor platform for ascorbic acid detection in human urine[J], *Chemosensors*, 2022, **10**(7), 268.

46 Y. H. Chi, An ultrasensitive photoelectrochemistry sensor for ascorbic acid based on etching perylenediimide modified CoOOH nanosheets, *Mater. Express*, 2019, **9**(7), 741–748.

47 H. Li, Q. Gao, L. Chen, *et al.*, Photocurrent determination ascorbic acid using an n-silicon electrode modified by platinum and cobalt hexacyanoferrate films, *Sens. Actuators, B*, 2012, **173**(10), 540–546.

48 R. M. Motaghed, L. Ge, H. Jiang, *et al.*, A facile photoelectrochemical sensor for high sensitive ROS and AA detection based on graphitic carbon nitride nanosheets, *Biosens. Bioelectron.*, 2018, **107**, 54.